




Monolithic integration of InP nanowires with CMOS fabricated silicon nanotips wafer

Anagha Kamath ^{1,*}, Oliver Skibitzki,² Davide Spirito ², Shabnam Dadgostar,³ Irene Mediavilla Martinez ³, Martin Schmidbauer,⁴ Carsten Richter,⁴ Albert Kwasniewski,⁴ Jorge Serrano,³ Juan Jimenez,³ Christian Golz,¹ Markus Andreas Schubert,² Jens W. Tomm,⁵ Gang Niu,⁶ and Fariba Hatami^{1,†}

¹*Institut für Physik, Humboldt Universität zu Berlin, Newtonstr.15, 12489 Berlin, Germany*

²*IHP-Leibniz Institut für Innovative Mikroelektronik, Im Technologiepark 25, 15236 Frankfurt (Oder), Germany*

³*GdS Optronlab, Universidad de Valladolid, Ed. LUCIA, Paseo de Belén 19, 47011 Valladolid, Spain*

⁴*Leibniz Institut für Kristallzüchtung, MaxBornStr.2, 12489 Berlin, Germany*

⁵*Max-Born-Institut für Nichtlineare Optik und Kurzzeitspektroskopie, Max-Born-Str. 2A, 12489 Berlin, Germany*

⁶*Key Laboratory of the Ministry of Education & International Center for Dielectric Research, School of Electronic Science and Engineering & The International Joint Laboratory for Micro/Nano Manufacturing and Measurement Technology, Xi'an Jiaotong University, Xi'an 710049, China*



(Received 13 April 2023; revised 23 August 2023; accepted 2 October 2023; published 19 October 2023)

The integration of both optical and electronic components on a single chip, despite several challenges, holds the promise of compatibility with complementary metal-oxide semiconductor (CMOS) technology and high scalability. Among all candidate materials, III-V semiconductors exhibit great potential for optoelectronics and quantum-optics based devices, such as light emitters and harvesters. The control over geometry, and dimensionality of the III-V nanostructures, enables one to modify the band structures, and hence provide a powerful tool for tailoring the optoelectronic properties of III-V compounds. One of the most creditable approaches towards such growth control is the combination of using a patterned wafer and the self-assembled epitaxy. This work presents monolithically integrated catalyst-free InP nanowires grown selectively on Si nanotip-patterned, CMOS compatible (001) Si substrates using gas-source molecular-beam epitaxy. We use nanoheteroepitaxy approach to selectively grow InP nanowires on Si nanotips, which holds benefits due to its peculiar substrate design. In addition, our methodology allows the switching of dimensionality of the InP structures between one-dimensional nanowires and three-dimensional bulklike InP nanoislands by thermally modifying the shape of silicon nanotips surrounded by the silicon dioxide layer during the thermal cleaning of the substrate. The structural and optical characterization of nanowires indicates the coexistence of both zincblende and wurtzite InP crystal phases in nanowires. The two different crystal structures were aligned with a type-II band alignment. The luminescence from InP nanowires was measured up to 300 K, which reveals their promising optical quality for integrated photonics and optoelectronic applications.

DOI: [10.1103/PhysRevMaterials.7.103801](https://doi.org/10.1103/PhysRevMaterials.7.103801)

I. INTRODUCTION

In recent years there has been substantial interest in monolithically integrating III-V semiconductors with silicon (Si) due to their extensive applications in electronics [1,2], optoelectronics [3–5], and photonics [6,7]. In particular, indium phosphide (InP) nanowires (NWs) have drawn attention due to their carrier lifetime between 120 ps and 2 ns [8,9], low surface recombination velocity of about 170 cm s^{-1} [10], and high carrier mobility around $1500 \text{ cm}^2 \text{ V}^{-1} \text{ s}^{-1}$ at room temperature [1], properties that render them outstanding for both light emission and light-harvesting applications. Due to their emission in near-infrared regions, InP NW-based devices can be used for short-distance optical fiber communications, free-space optics, and chip-to-chip optical interconnections [11]. Other widespread applications of InP NWs include photodetectors [12], tunnel diodes [13], solar cells [14], lasers [15], and photonic integrated circuits [11].

A common method for epitaxial growth of III-V NWs is selective area growth (SAG). This approach positions nanostructured openings on amorphous masks, for, e.g., silicon dioxide (SiO_2) over a substrate, and enables selective growth of NWs inside these openings. SAG mostly uses catalysts, such as gold particles of diameter 20–50 nm, which form liquid alloys with growth precursors and promote the growth of NWs [16,17]. Very often, the metal contamination incorporated at the interface of the catalyst and NW results in deep-level defects. For better device performance, it is crucial to avoid the formation of such defects. Therefore, catalyst-free growth is preferred [18,19].

Another developed methodology to integrate heterogeneous III-V nanostructures with Si substrate is the nanoheteroepitaxy (NHE) approach. Here, the III-V compound grows on a prepatterned Si nanotip (NT). The key advantages of NHE are (i) it is highly site specific, (ii) it facilitates reduction of the strain energy in III-V structures by distributing it in three dimensions through compliance effect [4,18–20], and (iii) it suppresses contamination segregation between III-V and Si due to a smaller contact area interface, thus minimizing the effects of lattice mismatching.

*kamathan@physik.hu-berlin.de

†hatami@physik.hu-berlin.de

Growth of fully relaxed three-dimensional bulklike InP nanoislands on freestanding Si NTs by NHE has been reported previously [21–23]. The present paper presents a method to modify thermally the shape of the Si NTs and use them for the nucleation and selective growth of monolithic and catalyst-free InP NWs on Si. The InP NWs are grown on prepatterned (001)-oriented Si NT substrates embedded within SiO₂ using gas-source molecular-beam epitaxy (GS-MBE). The distinctive geometry of the Si NTs substrate was processed by state-of-the-art CMOS nanotechnology. The characterization of structural and optical properties of these InP NWs demonstrates the coexistence of two different crystal structures, zincblende (ZB) and wurtzite (WZ) InP, aligned with a type-II band alignment. The NWs show room-temperature luminescence demonstrating their high optical properties.

II. METHODOLOGY AND SETUP

The Si NTs were fabricated using a state-of-the-art pilot line capable of 0.13- μm bipolar complementary metal-oxide semiconductor (BiCMOS) technology on 200-mm Si (001) wafer [24]. An on-axis oriented Si wafer was covered with a hard mask consisting of 120-nm thermal SiO₂ and 20-nm Si₃N₄ deposited by a low-pressure chemical vapor deposition batch reactor, followed by a 335-nm photoactive resist spin coated on top of the hard mask. The wafer was then etched using reactive ion etching to obtain arrays of Si NTs, subsequently opening the areas without resist. The Si NTs were completely covered in 1100-nm undoped silicon glass and 500-nm tetraethylorthosilicate plasma-enhanced chemical vapor deposition oxides. Finally, a chemical-mechanical polishing process was carried out to reduce the SiO₂-layer thickness, opening a circular Si-(001) NT surface with a diameter of 40–70 nm. The InP nanostructures were grown on Si NTs substrates in a GS-MBE Riber 32-P system using solid-source indium and thermally cracked phosphine.

Before transferring the Si substrates into the MBE system, the substrates were chemically cleaned using piranha solution and were dipped in diluted hydrogen fluoride (HF), to remove the top layer of SiO₂ from the surface of the tips (for more details see Ref. [4]).

The structural properties and the surface morphology of InP NWs were characterized by scanning electron microscopy (SEM, Pioneer two, Raith Fabrication), atomic force microscopy (AFM, Bruker Dimension Icon), scanning-transmission electron microscopy (STEM, FEI Tecnai Osiris operating at 200 kV), x-ray diffraction (XRD, XRT 3003 TT, GE Inspection Technologies), and Raman spectroscopy (HORIBA Jobin Yvon LABRAM HR 800 UV Raman spectrometer).

STEM lamellas were prepared by milling and undercutting processes using a Zeiss NVision 40 focused ion beam operating at up to 30 kV. XRD measurements were performed with a theta-theta x-ray-powder diffractometer in Bragg-Brentano geometry using Cu K α radiation ($\lambda = 1.542 \text{ \AA}$). To obtain information on the crystallographic phases within the NWs, $2\theta/\theta$ scans were recorded over a sufficiently large angular range. The corresponding crystal orientations of the ZB and WZ phases within the InP NWs were determined by pole figures carried out at selected WZ and ZB Bragg reflections.

For micro-Raman (μ -Raman) spectroscopy, a grating of 2400 lines per millimeter, and a solid-state laser with a wavelength of $\lambda = 532.8 \text{ nm}$ were used. The nominal laser power on the sample was below 1 mW, with an approximate irradiance of 100 kW cm^{-2} . Single NWs were extracted from Si tips by ultrasonication in ethanol solution and were then transferred to a foreign Si substrate for measurement. This substrate had been previously coated with a 100-nm gold layer to enhance the heat dissipation of NWs during the μ -Raman experiments.

The optical properties and carrier dynamics were characterized using temperature dependence and power-excitation dependence microphotoluminescence (μ -PL), time-resolved photoluminescence (TRPL), and cathodoluminescence (CL) spectroscopy. The μ -PL spectra were collected with a spectrometer (HORIBA i-hr320) equipped with a 1200-lines per millimeter grating and a Si charge-coupled device (CCD) for detection. The excitation source was a He-Cd laser (325 nm). The temperature was controlled in the range of 80–300 K. The TRPL measurements were conducted using a frequency-doubled Ti:sapphire laser at 403 nm at 5 K and the emission was detected using a 0.25- μm -grating monochromator and a Hamamatsu synchroscan streak camera. The pulse length was approximately 100 fs, operating at a repetition rate of 80 MHz. The laser was focused onto the sample with a spot diameter of 150 μm , which results in a high excitation density of about 10^7 W cm^{-2} during a single pulse. The CL measurements were carried out in an LEO 1530 (Carl Zeiss) field-emission SEM equipped with a MonoCL2 (Gatan, Oxford, UK) CL system. The detection was performed with a photomultiplier for the panchromatic CL images and a Peltier-cooled CCD detector for spectral acquisition.

III. RESULTS AND DISCUSSION

The Si NTs substrates were first baked in the pregrowth chamber of the MBE system at 200 °C to remove water-based contamination and other organic molecules. Subsequently, the substrates were transferred to the growth chamber and thermally cleaned, in order to remove native oxides and to modify the shape of the freestanding tips. At 750 °C the oxide layer is desorbed and the substrate can be used for selective growth of three-dimensional (3D) zincblende InP nanoislands on Si NTs, as we previously reported (Refs. [22–24]). At higher temperatures, a chemical reaction between Si tips and surrounded SiO₂ occurs which results in volatile by-product SiO [25,26] and resulting in a change in the shape of Si tips, flattening them out. At 800 °C the freestanding tips disappear fully and the tips are embedded in SiO₂. In such a way, voids with $190 \pm 15\text{-nm}$ depth and $60 \pm 10\text{-nm}$ opening form. The buried Si NTs can be used for catalyst-free and selective epitaxy of InP nanowires on Si. After the formation of the voids, the substrate temperature was reduced to 485 °C for the growth of InP NWs with the indium growth rate of 0.1 nm s^{-1} and phosphine flux of 4 sccm. The indium and phosphine were supplied simultaneously for the growth of the InP. Using this way of creating voids during thermal cleaning, one can switch from the growth of 3D InP nanoislands to 1D InP nanowires on the same type of CMOS-compatible Si wafer.

Figure 1 presents the images of a sample after the necessary steps for the growth of InP NWs. Figure 1(a) shows the 3D

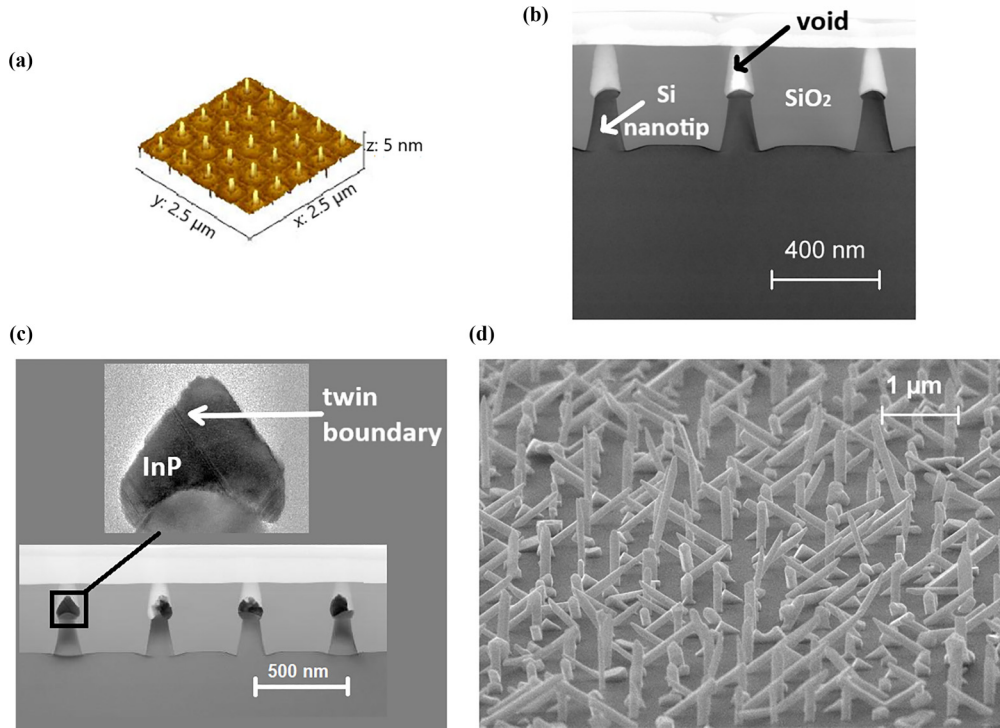


FIG. 1. (a) Three-dimensional AFM image after HF cleaning of matrix of Si NTs (001) embedded in SiO₂ layer. (b) Cross-sectional STEM image of sample after thermal cleaning. Voids (white part) are formed on top of Si NTs (dark gray) during thermal cleaning. (c) Cross-sectional STEM image indicates nucleation of InP NW (black) inside voids on Si NTs after 50 min of growth. Inset shows cross-sectional STEM image indicating twin boundary defects during nucleation of InP. (d) Cross-sectional (tilted 80°) SEM image of selective growth of InP NWs after 150 min of growth.

AFM image of the exposed Si NT (001)- SiO₂ substrate after cleaning with HF dip. The cross-sectional STEM image of the thermally cleaned Si NTs at 800 °C is shown in Fig. 1(b). Due to the nonuniform chemical reaction between Si NTs and SiO₂ during thermal cleaning, voids with different shapes are formed, as shown in Fig. 1(b). The nucleation of InP NWs takes place selectively and catalyst-free inside these voids. Figure 1(c) displays the cross-sectional STEM of a sample after 50 min of growth. The high-resolution STEM image indicates the twin boundary in the InP nanocrystals [Fig. 1(c), inset]. As per the literature, when the ZB crystal structure has a rotational twin of 180°, it gives rise to a single WZ unit cell and similarly, a rotational twin of 180° in the WZ structure would give rise to a ZB unit cell [27,28]. The shape of the InP nanocrystals within the voids differs, which depends on the size and aspect ratio of voids, and the contact angle of InP seed. If the deposition continues, InP grows out of the voids as NWs with different orientations [29,30]. Figure 1(d) portrays a cross-sectional (tilted 80°) SEM image of an ensemble of InP NWs after 150 min of growth. The quantitative analysis based on the SEM investigation using IMAGEJ software [31] shows that InP NWs are present on 77% of Si NTs. The height of the NWs varies from 200 to 1400 nm and the diameter is between 60 and 180 nm. In addition, 37% of the NWs are aligned in the [001] direction and others are aligned with an angle between 33° and 80° to the (001) plane.

In order to investigate the crystal properties of the nanowires, XRD measurements were performed on a large array of NWs. Figure 2 shows an x-ray 2θ/θ scan over a wide

angular range. In addition to the strong Si (004)_{Si} reflection (and the “basis”-forbidden Si (002)_{Si} reflection [32]), comparatively weak Bragg reflections from the InP NWs can be observed.

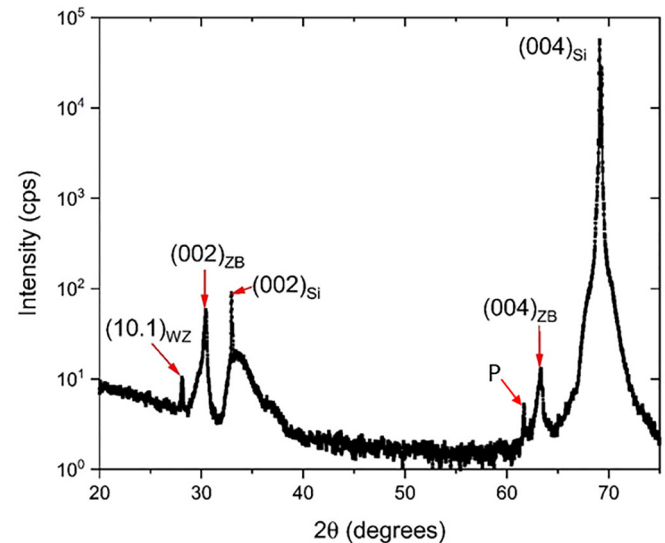


FIG. 2. X-ray 2θ/θ scan shows both ZB and WZ Bragg reflections from ensemble of nanowires. Peaks at 30.42° and 63.30° are related to InP (002)_{ZB} and (004)_{ZB}, indicating (001)_{ZB} orientation of ZB phases within InP NWs. Peak at 28.07° corresponds to (10.1)_{WZ}. Weak peak at 61.69° (P) is due to (004)_{Si} substrate Bragg reflection excited by Cu Kβ radiation.

In particular, the peaks at $2\theta = 30.42^\circ$ and $2\theta = 63.30^\circ$ in Fig. 2 correspond to the $\text{InP } (002)_{\text{ZB}}$ and $(004)_{\text{ZB}}$ ZB Bragg reflections, respectively, indicating a $(001)_{\text{ZB}}$ orientation of the ZB phases. This epitaxial relationship is expected for the growth of cubic InP on cubic (001) Si substrate. From the experimental 2θ values a vertical lattice parameter of $a_{\text{ZB}} = 5.8765 \text{ \AA}$ can be determined. This value is very close to the lattice parameter reported for bulk ZB InP ($a = 5.8687 \text{ \AA}$ [33]) indicating a negligible strain of 0.1%. Furthermore, a weak peak is observed at $2\theta = 28.07^\circ$ which fits to the $(10.1)_{\text{WZ}}$ WZ Bragg reflection. The corresponding experimental net-plane spacing $d_{10.1} = 3.179 \text{ \AA}$ is slightly smaller than the value $d = 3.224 \text{ \AA}$ of bulk InP WZ when using the lattice parameters $a = 4.150 \text{ \AA}$ and $c = 6.777 \text{ \AA}$ as reported in Ref. [34]. The obtained lattice parameters for WZ InP as calculated from reciprocal-space mapping are $a = 4.14 \text{ \AA}$ and $c = 6.81 \text{ \AA}$, indicating the strain values of $\varepsilon_{xx} = -0.2\%$ and $\varepsilon_{zz} = +0.6\%$. Note that the weak peak at $2\theta = 61.69^\circ$ (labeled “P”) represents the $(004)_{\text{Si}}$ substrate Bragg reflection excited by Cu $K\beta$ radiation ($\lambda = 1.392 \text{ \AA}$).

Due to the fact that the peak equivalent to the WZ Bragg reflection at $2\theta = 28.07^\circ$ is weak, further measurements are required. We therefore measured XRD pole figures of selected Bragg reflections (Fig. 3). Although the hexagonal WZ phase does not intrinsically show a fourfold symmetry, it is striking that all experimental pole figures exhibit a fourfold in-plane symmetry. This is due to the symmetry of the underlying Si (001) surface, leading to four equivalent in-plane orientations of the InP NWs, each rotated by 90° about the surface normal.

Figure 3(a) shows a pole figure taken using the $\text{InP } (002)_{\text{ZB}}$ Bragg reflection ($2\theta = 30.42^\circ$) conditions. The strong central peak confirms that ZB InP exhibits prevailing $(001)_{\text{ZB}}$ orientation and is therefore aligned along the $[001]_{\text{Si}}$ surface normal. In order to determine the epitaxial relationship between the ZB and WZ phases more precisely, it is useful to first have a look at the pole figure taken at $2\theta = 25.76^\circ$. Here, both the $(111)_{\text{ZB}}$ and $(0002)_{\text{WZ}}$ Bragg reflections can be observed. Since the $(111)_{\text{ZB}}$ and $(0002)_{\text{WZ}}$ net planes in the InP NWs are the domain boundaries between the phases, the intensity pattern displayed in Fig. 3(b) does not show any splitting between the $(111)_{\text{ZB}}$ and $(0002)_{\text{WZ}}$ Bragg reflections (marked by white circles).

However, in the pole figure taken at the $(10.1)_{\text{WZ}}$ Bragg reflection at $2\theta = 28.07^\circ$ [Fig. 3(c)], four central peaks can be observed, each tilted away from the pole by about 5° . This value is very close to the expected value of 7.4° , which is the angle between the $(001)_{\text{ZB}}$ and the $(10\bar{1})_{\text{WZ}}$ planes for bulk ZB and WZ sharing a common $(111)_{\text{ZB}}/(0002)_{\text{WZ}}$ plane. Note again that the observed fourfold symmetry is caused by the fourfold in-plane orientation of the NWs. The arrangement of the other $\{10.1\}_{\text{WZ}}$ Bragg peaks [marked by white circles in Fig. 3(c)] is also mediated by the fourfold symmetry of in-plane NW orientation.

The pole figures presented in Fig. 3 prove the coexistence of the cubic ZB and hexagonal WZ phases in an ensemble of NWs and show the epitaxial relationship between them and the underlying Si substrate. Furthermore, beyond the strong peaks discussed so far, additional weaker peaks can be observed in all pole figures. For example, in the case of ZB InP [Fig. 3(a)] the central $(002)_{\text{ZB}}$ Bragg peak is surrounded

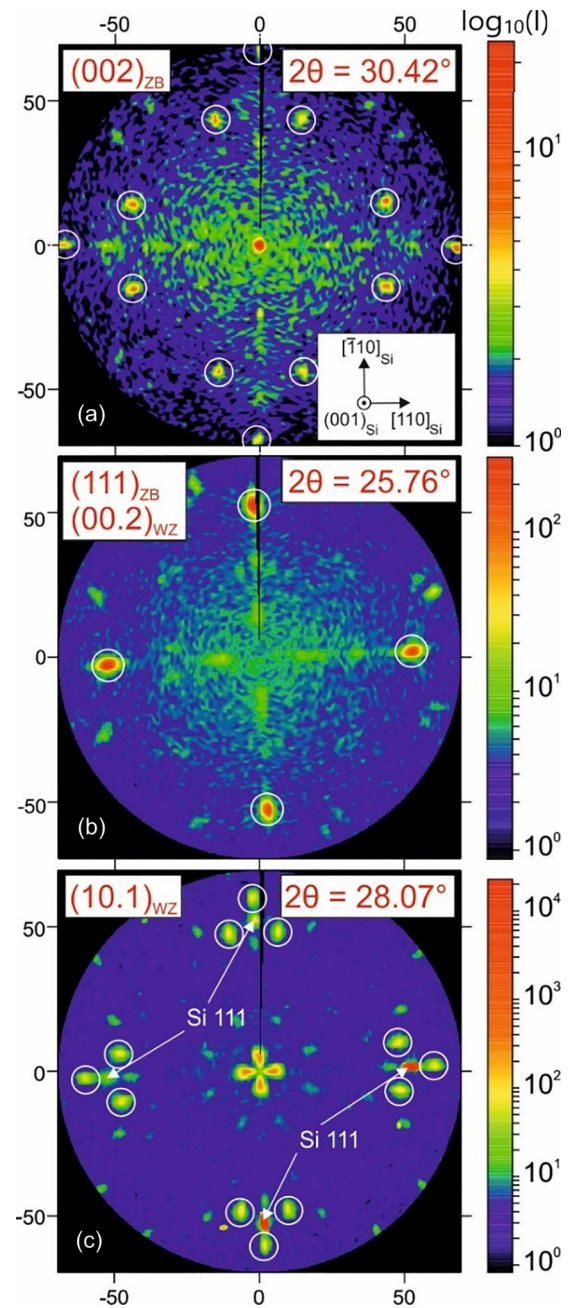


FIG. 3. X-ray pole figures measured at (a) $2\theta = 30.42^\circ$, (b) $2\theta = 25.76^\circ$, and (c) $2\theta = 28.07^\circ$. Inset shows crystallographic orientation of the underlying Si (001) substrate is indicated. Intensity (cps) is plotted on a logarithmic scale; see color bar on right.

by 12 additional peaks of about the same intensity (marked by white circles). These additional peaks are due to 180° rotational twinning of ZB (sphalerite) InP; see, e.g., Ref. [35]. Likewise, also the pole figures showing WZ Bragg reflections [e.g., Fig. 3(c)] exhibit additional weak peaks which are related to twinning. The rotational twins in ZB and WZ structures are formed when they are rotated by 180° around their corresponding $\langle 111 \rangle$ growth direction, giving rise to the form WZ and ZB structures, respectively [36]. Using the x-ray pole figures, we could show the coexistence of the cubic ZB and hexagonal WZ phases in the InP NW ensemble.

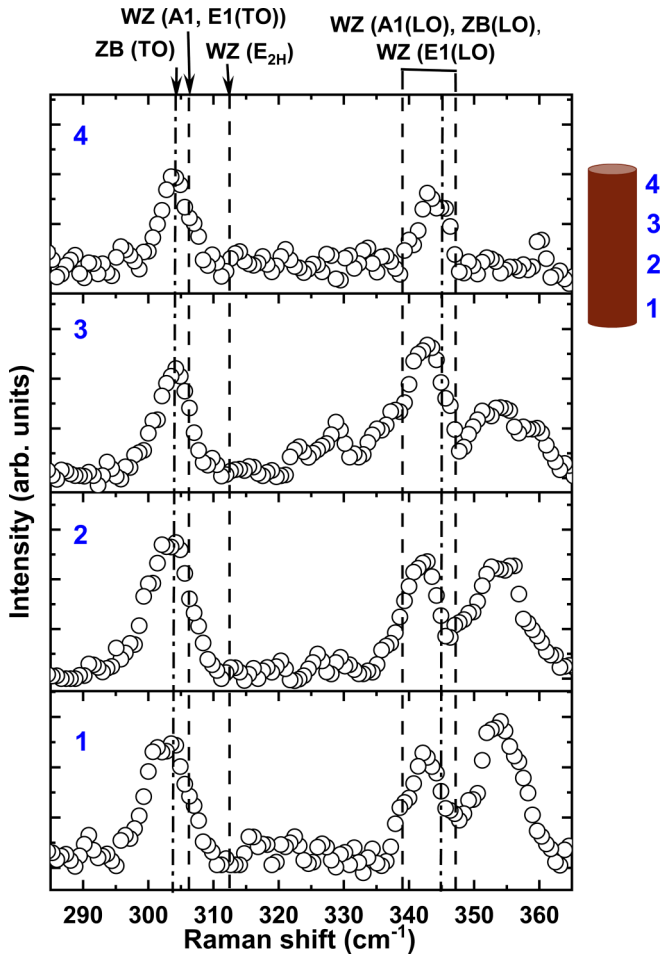


FIG. 4. Micro-Raman point spectra of extracted InP NW at four different sections of wire. On right side of spectra is schematic of extracted single InP NW indicating different positions of the measurement. Point 1 and 4 are from two ends, while points 2 and 3 are from middle sections of NW. Dashed line shows expected vibrational modes of bulk ZB and bulk WZ InP.

The capability of having different crystal structures within the NW is known as polytypism. ZB crystal structure is formed by interpenetration of two fcc Bravais lattices, while WZ is constructed by interpenetration of two hexagonal-close-packed lattices. Nine out of the 12 nearest-neighbor atoms of WZ are at the same crystallographic positions as that of ZB, while the other three are responsible for the hexagonal structure of WZ. Due to these structural similarities between the two crystal structures, their crystal potentials are very similar and the phonon energies are close to each other. However, the ZB crystal structure is characterized by the T_d^2 space group and the WZ crystal structure belongs to the C_{6v}^4 space group. Within the T_d^2 group, the only Raman-active vibrational representation is F_2 . In contrast, the C_{6v}^4 group permits multiple Raman-active modes, namely the A_1 , E_1 , E_{2H} , and E_{2L} representations. The vibrational modes, F_2 , A_1 , and E_1 modes undergo splitting into longitudinal optical (LO) and transverse optical (TO) components. Thus, the difference in the crystal phases is reflected in the optical vibrational modes. Considering this distinguishable property, we investigated the

TABLE I. Reported optical phonon modes of bulk ZB (Refs. [37,39]) and bulk WZ InP (Ref. [38]) as reported in the literature.

Crystal phase of InP	Modes	Reported $\omega(\text{cm}^{-1})$
ZB	$F_2(\text{TO})$	303 [37,39]
ZB	$F_2(\text{LO})$	345 [37,39]
WZ	$A_1(\text{TO})$, $E_1(\text{TO})$	305.3 [38], 306.3 [38]
WZ	$A_1(\text{LO})$, $E_1(\text{LO})$	347 [38], 339 [38]
WZ	E_{2H}	313 [38]

spatial distribution of the crystal phases within a single InP NW using micro-Raman spectroscopy.

Figure 4 shows the Raman point spectra of an extracted single InP NW at different sections of the NW at room temperature. Spectra No. 1 and No. 4 are from the ends of the NW while spectra No. 2 and No. 3 comprise the middle section of the NW. The dashed vertical lines in Fig. 4 show the position of expected Raman modes of bulk ZB and WZ InP, as summarized in Table I [37–39]. The differentiation between $A_1(\text{TO})$ and $E_1(\text{TO})$ modes, $A_1(\text{LO})$ and $E_1(\text{LO})$ modes, and E_{2H} modes of WZ InP is significantly challenging.

This challenge arises primarily because the measurement is not polarized dependent, causing the modes to overlap. However, as we progress from segment 1 to segment 4 along the NW, there is a notable evolution in the Raman spectrum. Specifically, the peak positions exhibit shifts, and new peaks, such as those prominent in segment 3, emerge. Such behavior is characteristic of mixed-phase structures, where domains of different crystalline phases coexist. A possible explanation for these observations is the coexistence of ZB and WZ structures within the NW, as reported for example in Refs. [37,40].

It is well known that strain and defects can induce shifts in vibrational modes. According to the XRD and TEM results, the NWs contain defects, and the WZ phase is slightly strained. The Raman spectra confirm these results and indicate that the NW comprises both ZB and WZ crystal structures. The peak at approximately 355 cm^{-1} and above may be caused by multiphonon, with the acoustic mode contributing. It is quite challenging to determine the source of the signal, though, because the NWs have a complex structure and numerous modes are adjacent to one another.

Now, we focus on the electronic structures and optical properties of the InP NWs. The resemblance of atomic arrangements in the ZB and WZ InP results not only in similar energies for the phonons but also in the band-gap energies being close to each other. The 0 K band gap for bulk ZB InP is 1.42 eV [41] and the calculated band gap of WZ InP is 1.47 eV [42]. However, the reported experimental low-temperature band-gap energy of the WZ structure based on InP NWs ranges from 1.47 to 1.49 eV [43]. Most of the reported InP NWs have a polytype structure. However, the InP NWs with a diameter of less than 40 nm are found in pure WZ crystal structure [44,45]. The ratio of the facet area to the NW volume can be used to determine the structural stability of NWs from a thermodynamic perspective [44].

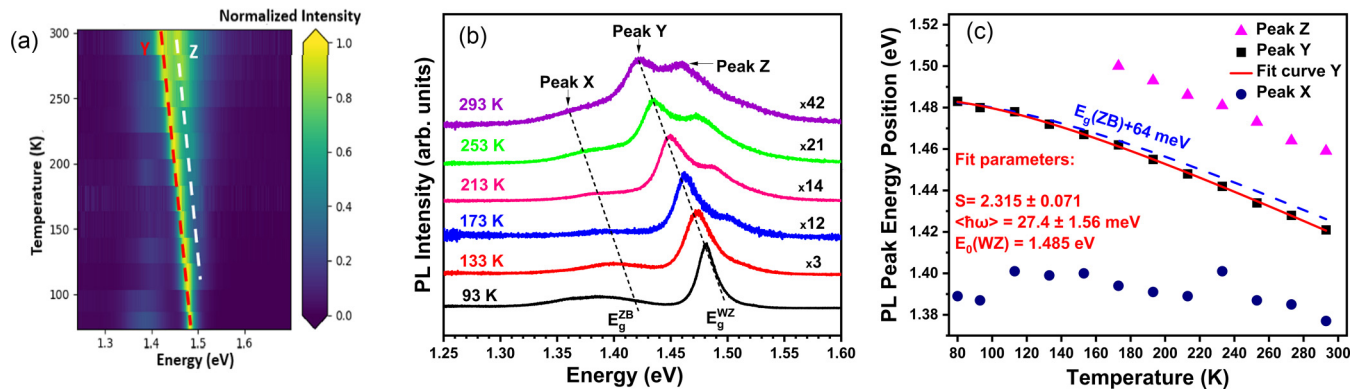


FIG. 5. (a) Two-dimensional contour plot of normalized temperature-dependent μ -PL spectra from 80 to 293 K measured using 325-nm laser with 0.1-mW excitation power. Two dominant peaks, peak Y and peak Z, can be distinctly observed and are represented using red and white dashed lines, respectively. Evolution of peaks is depicted using dashed lines. (b) Selected PL spectra from contour plot (a). Three peaks are identified, namely, peaks X, Y, and Z. Dashed line shows expected energy positions of bulk ZB and WZ at corresponding temperatures. (c) Temperature dependence of energy position of peak X, peak Y, and peak Z. Data for peak Y are fitted by temperature-dependent band-gap model based on electron-phonon coupling as described by Eq. (1) (red line). Fit parameters are similar to material parameters of WZ InP. For comparison, blue dashed line shows temperature dependency of the band gap of ZB InP with offset of 64 meV.

Additionally, the relative stability of the system is given by $\Delta E = E_{\text{WZ}} - E_{\text{ZB}}$, where E_{WZ} and E_{ZB} are the formation energies of WZ and ZB NWs, respectively. For NWs with smaller diameters, ΔE is negative, which means NWs are exclusively stabilized in WZ form. With an increase in the diameter of NW, ΔE increases to a positive value which leads to the appearance of both WZ and ZB crystal structures in the NW. For very large diameters, ΔE converges to the energy of bulk III-V crystal indicating a predominance of ZB crystal structure [44,46,47]. Thus, one of the ways by which crystal structure is engineered is by adjusting the diameter of the NWs, consequently modifying the optical properties of the material.

Figure 5(a) shows the 2D contour plot of normalized μ -PL intensity between 80 and 293 K measured using a 325-nm laser with 0.1-mW power. The laser beam irradiates a region with a maximum of four NWs due to their spot diameter, which is around 700 nm. Figure 5(b) shows the selected spectra from the contour plot of Fig. 5(a). Three peaks, labeled peak X, peak Y, and peak Z, can be distinctly observed. At 93 K, the energy of broad peak X is centered at 1.38 eV. The highest-intensity peak corresponds to peak Y, centered at 1.48 eV. With the increasing temperature above 130 K, a high-energy peak labeled peak Z appears and its intensity gradually increases with rising temperature.

Figure 5(c) shows the energy positions of the peaks versus the temperature. Peak Z shifts to lower energy of about 40 meV from 1.5 eV (at 173 K) to 1.46 eV (at 293 K). Peak Y shifts also to lower energies with increasing temperature from 1.48 eV (at 93 K) to 1.42 eV (at 293 K) and shows a total redshift of about 60 meV. The position of peak Y between 80 and 293 K is fitted by the temperature-dependent band-gap equation based on electron-phonon coupling [Eq. (1)] developed by O'Donnell and Chen [48],

$$E_g(T) = E_0 - S\langle \hbar\omega \rangle \left(\coth \left(\frac{\langle \hbar\omega \rangle}{2k_B T} \right) - 1 \right), \quad (1)$$

where $E_g(T)$ is the band gap at temperature T , E_0 is the band gap at 0 K, S is the Huang-Rhys factor, which is a measure of

the strength of electron-phonon coupling, $k_B T$ is Boltzmann thermal energy, and $\langle \hbar\omega \rangle$ is average phonon energy. According to this equation, the band-gap behavior is governed by the S and $\langle \hbar\omega \rangle$ values. The obtained values of S and $\langle \hbar\omega \rangle$ from the fitting curve (red curve) are 2.315 and 27.4 meV, respectively, which are in good agreement with the literature values of WZ InP [49]. Although the strength of electron-phonon coupling (S) and average phonon energy ($\langle \hbar\omega \rangle$) do not vary much for WZ and ZB InP due to the similarity in their crystal structures, as discussed earlier, the behavior of the curves at higher temperatures, where the phonons play a dominant role, is comparable. For a better comparison with the measured data, we plotted the temperature-dependent band gap for ZB InP with an offset of 64 meV (blue-dashed curve). The energy position of peak Y and its thermal behavior match very well with the band-to-band transition of WZ InP. We therefore attribute peak Y to WZ InP. Note that the determined value of 1.485 eV for E_0 may slightly deviate from the band-gap energy at 0 K, due to lack of data at that temperature range.

Peak Z is 50 meV higher than peak Y and follows a similar trend of temperature-dependent band-gap behavior as that of peak Y as shown in Fig. 5(c). Similar peaks have been previously reported at higher temperatures which gradually decrease in intensity as the temperature decreases [50,51]. According to the reported PL excitation measurements, this peak can be related to the transition from CB of WZ InP (Γ_{7C}) to light-hole split-off valence band (Γ_{7V}) [43,51].

The position of peak X located at 1.38 eV does not vary much with the temperature. The total shift in the energy position from 80 to 293 K is 12 meV, as shown in Fig. 5(c).

Figure 6(a) shows the μ -PL spectra for different excitation power at 80 K. The laser power was controlled with optical density filters in the range of 0.001 to 10 mW. Two prominent peaks can be resolved for all excitation powers. A sharp peak occurs at 1.48 eV, similar to peak Y in Fig. 5(a), while a broad peak arising at 1.35 eV is similar to peak X.

Figure 6(b) shows the energy position of both peaks as a function of excitation power density. A large power-dependent

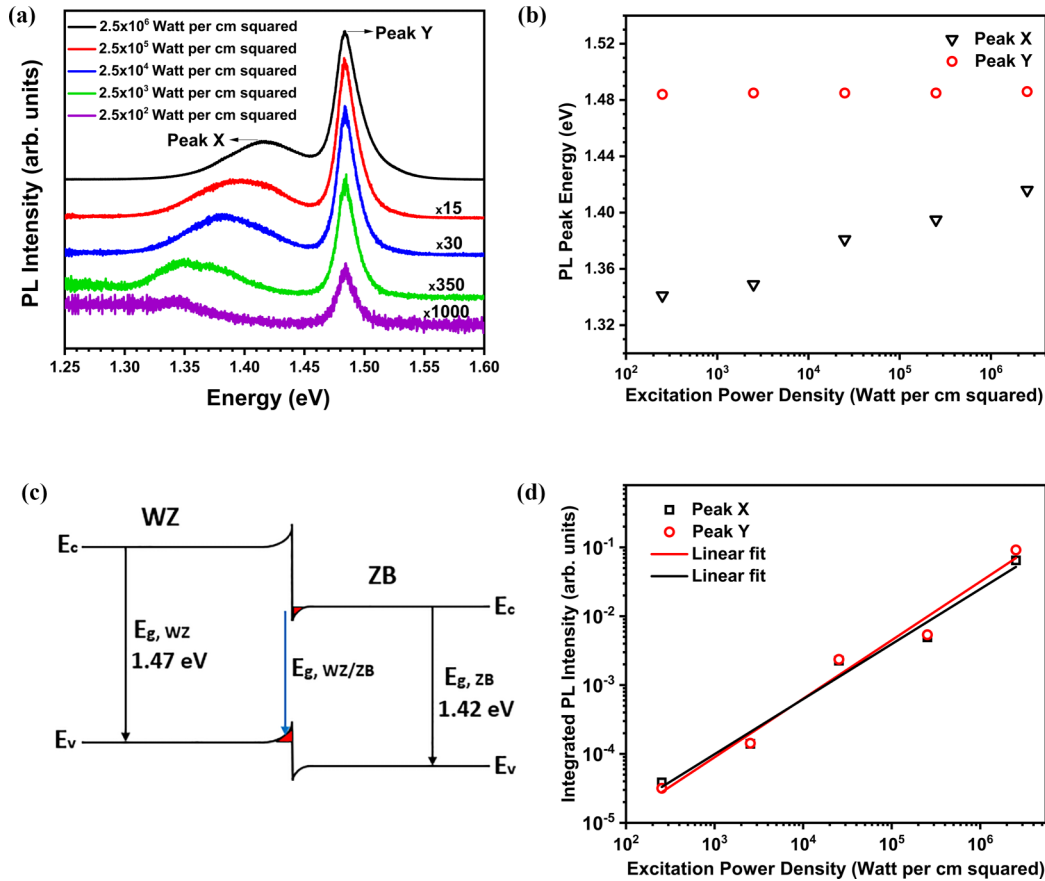


FIG. 6. (a) Excitation power density dependence PL spectra at 80 K. (b) Energy of peak X and peak Y as function of excitation power density. Large blueshift of 76 meV was measured for peak X. (c) Schematic of type-II band alignment at ZB and WZ InP heterointerface (not scaled) where electrons are confined in triangular potential well of CB in ZB InP and holes are confined in triangular potential well of VB in WZ InP. (d) Excitation power density dependency of total integrated intensity of peak X and peak Y.

blueshift of 76 meV is observed for peak X, whereas peak Y shows a slight blueshift of 2 meV when the power is increased from 2.5×10^2 to 2.5×10^6 W cm⁻². A large blueshift is mostly related to a type-II band alignment [49,52,53]. Type-II band alignment is predicted for ZB/WZ InP heterojunction with the conduction-band (CB) and valence-band (VB) offsets of WZ InP to be 129 and 45 meV higher, respectively, than the corresponding bands in ZB InP [42,54,55].

Figure 6(c) shows a nonscaled schematic of the type-II band alignment of the ZB/WZ heterointerface. The electrons are localized within the CB of the ZB structure, while holes are in the VB of the WZ crystal structure. The spatial separation of electrons and holes induces an electric field at the interface which causes the bands to bend [52]. As a result of band bending, there is a formation of a triangular potential well at the ZB/WZ heterointerface. By increasing the excitation density, the band-bending conditions are altered, narrowing the triangular potential well and thus pushing up the confined states [56]. The blueshift of peak X with increasing excitation density follows this behavior; therefore, we assign peak X to the electron-hole transition, where the electrons are confined in the triangular potential well of the CB in ZB InP and holes are confined in the triangular potential well of the VB in WZ InP.

The integrated μ -PL intensities for peak X and peak Y as a function of the excitation power density are plotted in Fig. 6(d). The intensity of both peaks increases linearly with the excitation power density with no sign of saturation in the applied range of the power density.

We further utilized TRPL to probe the dynamics of the carrier's recombination and gain more insight into the origin of the PL peaks. Figure 7(a) shows the temporal evolution of the PL spectrum of peak X and peak Y, observed at about 1.42 and 1.49 eV, similar to the steady-state PL spectra at low temperatures. Figure 7(b) shows the normalized time-resolved decay profile of peak X and peak Y, in a semilog axis. In order to gain a better understanding of the relative dynamics of the recombination processes of the two peaks, our focus here remained primarily on the initial segments of the decay curves. Hence, for a direct comparison, we employed a mono-exponential decay fitting.

The observed decay time for peak X is about 346 ps and for peak Y is about 224 ps. These values closely align with the previously reported decay time for the emission at the ZB/WZ heterointerface and WZ InP, respectively at high excitation density [56]. The slower decay time for peak X compared to peak Y can be explained by the spatial separation of electrons and holes due to type-II band alignment.

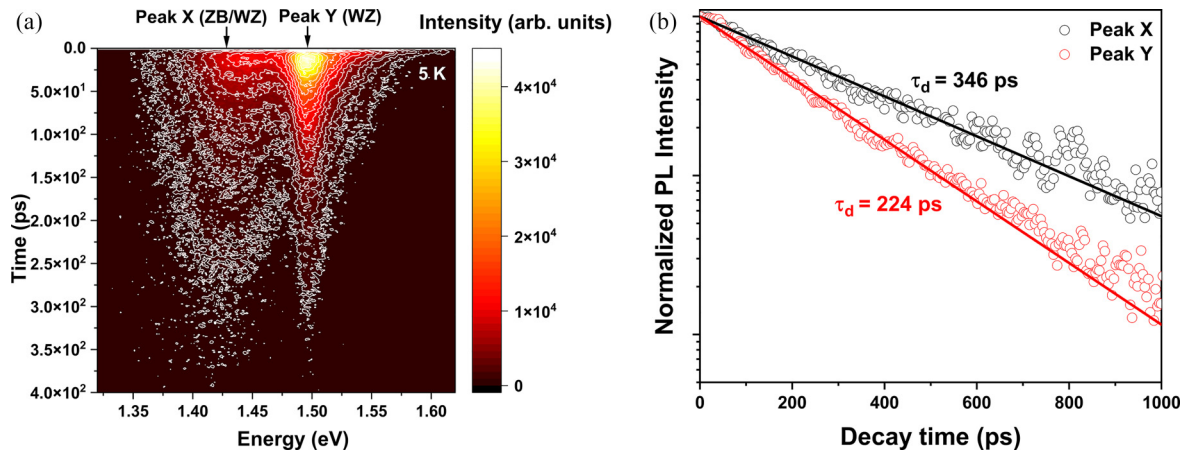


FIG. 7. (a) False-color map depicting temporal evolution of two peaks at 5 K at power-excitation density of 10^7 W cm^{-2} . (b) Time-resolved decay profiles of peak X and peak Y, each fitted using monoexponential decay model, show time decay of 346 and 224 ps, respectively.

To gain a better understanding of the luminescence transition within a single NW, CL measurements were carried out on selected NWs. In addition to higher spatial resolution than μ -PL, CL has the ability to obtain detailed depth-resolved information by varying the electron energy. Measurements were done at 88 K on different NWs. The spectra of the NWs typically show three to four peaks in the 1.36–1.50-eV range.

The CL spectra were recorded along the single NW as shown in Fig. 8(a). Figure 8(b) shows seven spectra recorded at different positions corresponding to the numbers specified in the panchromatic image of Fig. 8(a). The vertical dashed line represents the expected band-gap energy of bulk ZB and WZ crystal structures at 88 K. There is a peak at around 1.40 eV, which fits with the PL signal due to the transition from ZB/WZ heterointerface [peak X in Fig. 5(b)], and we therefore associate it with this transition. The highest-energy peak at around 1.46 eV is similar to peak Y in the PL spectra and its position matches the energy of the fundamental band gap of WZ InP. In addition to these peaks, we observe a

third peak at 1.43 eV. The energy of this peak aligns well with the expected band gap of ZB InP. The variation in the intensity of these three dominant peaks along the length of the NW is demonstrated in Fig. 8(c). The high spatial resolution of CL enables the detection of emissions from even minute ZB segments interspersed within the nanowires, revealing localized structural variations. This peak, alongside the type-II and WZ peaks, provides a more comprehensive view of the mixed-phase nature of these nanowires.

The distribution of the phases along the NW as obtained from the intensity of the different peaks is shown in Fig. 8(c). To explain the inhomogeneity observed in the CL, it is crucial to consider the coexistence of ZB and WZ crystal structures in the NW. The nonuniform variations in crystal structure and the resulting differences in the band structure can contribute to the spatially heterogeneous CL emission. One can observe that the central part of the NW is mostly WZ (spectra No. 3, No. 4, and No. 5), while both WZ and ZB phases coexist in the two ends of the NW (spectra No. 1, No. 2, No. 6, and No. 7).

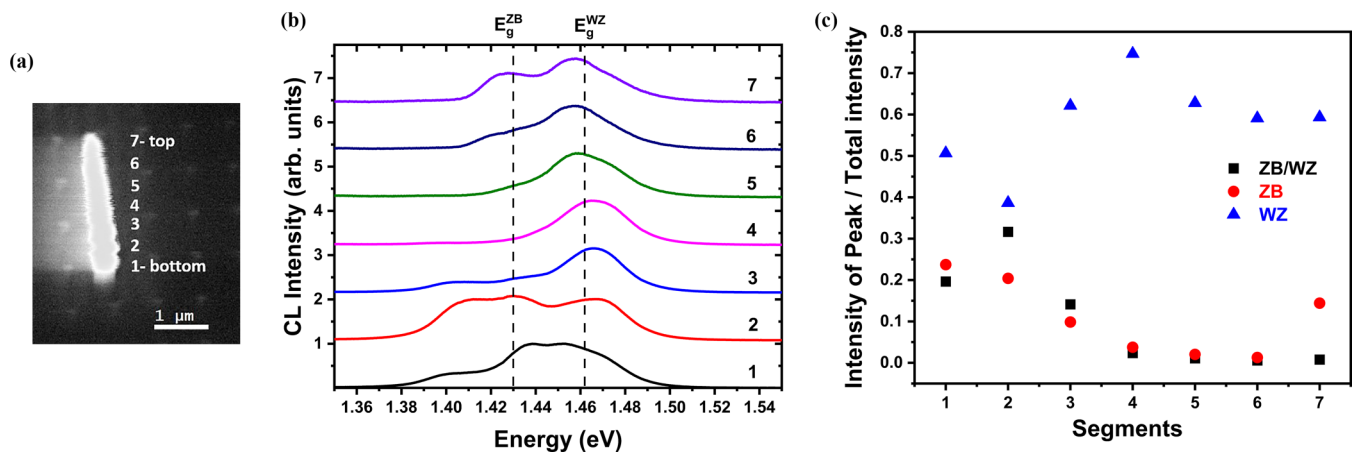


FIG. 8. (a) Panchromatic CL image of single InP NW at 88 K divided in seven segments from bottom to top. (b) CL spectra of seven segments of NW showing three peaks for each spectrum. Vertical dashed line shows expected band-gap energy peak of bulk ZB and WZ InP at 88 K. (c) Contribution of each peak in their respective spectrum and their tendency to grow in crystal phase at different positions of NW.

It is interesting to note that in the CL spectra, we observe the fingerprint of the ZB segments, which is in contrast to the PL spectra. The luminescence signals due to the WZ and ZB/WZ heterointerface are detectable using both methods. Although the transition at the interface requires the presence of both WZ and ZB crystal phases in the NW, the PL does not show any evidence of ZB band-to-band recombination. The reason may be the different orientations of the self-organized NWs and that the smaller ZB crystal phases could not be probed by the incident light. The intensity of light emission from both ZB and WZ crystal phases depends on the polarization of incident light and its selection rules [57]. In contrast to the PL measurements, for CL spectroscopy we use the polarization-independent electron beam to excite the sample. The higher spatial resolution of the CL is also beneficial for the detection of small ZB segments. Thus, the combination of PL and CL measurements helps to explain the optical transitions present in our polytype InP nanowires, capturing contributions from WZ, ZB, and the ZB/WZ heterointerface and fortifying our results from structural characterizations.

IV. CONCLUSION

In conclusion, we have demonstrated a sustainable and unique way to switch between the growth of relaxed InP nanoislands with pure ZB crystal structure and the polytype

ZB-WZ InP nanowires on a CMOS-compatible Si nanotips wafer. By adjusting the temperature during thermal cleaning of the substrate prior to growth, the shape of the Si tips was modified via a thermally triggered chemical reaction between SiO₂ and Si tips. Using GS-MBE and the nanoheteroepitaxy approach, catalyst-free InP nanowires were grown selectively. We have shown the presence of both WZ and ZB crystal structures in the ensemble, as well as in the single NWs, using a variety of different complementary experimental techniques, such as XRD, Raman, PL, and CL. The NWs exhibit luminescence in the range of 1.40 to 1.50 eV up to room temperature. The up-to-room-temperature luminescence of the single InP nanowires integrated monolithically on CMOS-compatible Si wafer demonstrates their promising optical quality for optoelectronic and integrated photonic applications.

The datasets used and/or analyzed during the current study are available from the corresponding author upon reasonable request.

ACKNOWLEDGMENTS

A.K. thanks Deutscher Akademischer Austauschdienst (DAAD) for her research grant. This work was supported by the German Research Foundation (DFG Grant No. 428250328).

-
- [1] X. Yan, B. Li, Q. Lin, P. Liu, Y. Luo, Q. Lu, X. Zhang, and X. Ren, High performance transistors and photodetectors based on self-catalyzed zinc-blende InP nanowires, *Appl. Phys. Lett.* **114**, 243106 (2019).
 - [2] K. Tomioka, T. Tanaka, S. Hara, K. Hiruma, and T. Fukui, III-V nanowires on Si substrate: Selective-area growth and device applications, *IEEE J. Sel. Top. Quantum Electron.* **17**, 1112 (2011).
 - [3] S. Mauthe, Y. Baumgartner, M. Sousa, Q. Ding, M. D. Rossell, A. Schenk, L. Czornomaz, and K. E. Moselund, High-speed III-V nanowire photodetector monolithically integrated on Si, *Nat. Commun.* **11**, 4565 (2020).
 - [4] G. Niu, G. Capellini, G. Lupina, T. Niermann, M. Salvalaglio, A. Marzegalli, M. A. Schubert, P. Zaumseil, H. M. Krause, O. Skibitzki *et al.*, Photodetection in hybrid single-layer graphene/fully coherent germanium island nanostructures selectively grown on silicon nanotip patterns, *ACS Appl. Mater. Interfaces* **8**, 2017 (2016).
 - [5] P. Krogstrup, H. I. Jørgensen, M. Heiss, O. Demichel, J. V. Holm, M. Aagesen, J. Nygard, and A. Fontcuberta i Morral, Single-nanowire solar cells beyond the shockley-queisser limit, *Nat. Photon.* **7**, 306 (2013).
 - [6] G. N. Malheiros-Silveira, F. Lu, I. Bhattacharya, T. T. D. Tran, H. Sun, and C. J. Chang-Hasnain, III-V compound semiconductor nanopillars monolithically integrated to silicon photonics, *ACS Photonics* **4**, 1021 (2017).
 - [7] T. Y. Chang, H. Kim, B. T. Zutter, W. J. Lee, B. C. Regan, and D. L. Huffaker, Orientation-controlled selective-area epitaxy of III-V nanowires on (001) silicon for silicon photonics, *Adv. Funct. Mater.* **30**, 2002220 (2020).
 - [8] T. T. T. Vu, T. Zehender, M. A. Verheijen, S. R. Plissard, G. W. G. Immink, J. E. M. Haverkort, and E. P. A. M. Bakkers, High optical quality single crystal phase wurtzite and zincblende InP nanowires, *Nanotechnology* **24**, 115705 (2013).
 - [9] H. J. Joyce, C. J. Docherty, Q. Gao, H. H. Tan, C. Jagadish, J. Lloyd-Hughes, L. M. Herz, and M. B. Johnston, Electronic properties of GaAs, InAs and InP nanowires studied by terahertz spectroscopy, *Nanotechnology* **24**, 214006 (2013).
 - [10] H. J. Joyce, J. Wong-Leung, C. K. Yong, C. J. Docherty, S. Paiman, Q. Gao, H. H. Tan, C. Jagadish, J. Lloyd-Hughes, L. M. Herz *et al.*, Ultralow surface recombination velocity in InP nanowires probed by terahertz spectroscopy, *Nano Lett.* **12**, 5325 (2012).
 - [11] Y. Ding, J. Motohisa, B. Hua, S. Hara, and T. Fukui, Observation of microcavity modes and waveguides in InP nanowires fabricated by selective-area metalorganic vapor-phase epitaxy, *Nano Lett.* **7**, 3598 (2007).
 - [12] X. Yan, B. Li, Y. Wu, X. Zhang, and X. Ren, A single crystalline InP nanowire photodetector, *Appl. Phys. Lett.* **109**, 053109 (2016).
 - [13] F. Zafar and A. Iqbal, Indium phosphide nanowires and their applications in optoelectronic devices, *Proc. Royal Soc. A: Math. Phys. Eng. Sci.* **472**, 20150804 (2016).
 - [14] H. Goto, K. Nosaki, K. Tomioka, S. Hara, K. Hiruma, J. Motohisa, and T. Fukui, Growth of core-shell InP nanowires for photovoltaic application by selective-area metal organic vapor phase epitaxy, *Appl. Phys. Express* **2**, 035004 (2009).
 - [15] L. C. Chuang, M. Moewe, S. Crankshaw, and C. Chang-Hasnain, Optical properties of InP nanowires on Si substrates

- with varied synthesis parameters, *Appl. Phys. Lett.* **92**, 013121 (2008).
- [16] J. Wang, S. Plissard, M. Hocevar, T. T. T. Vu, T. Zehender, G. G. W. Immink, M. A. Verheijen, J. Haverkort, and E. P. A. M. Bakkers, Position-controlled [100]InP nanowire arrays, *Appl. Phys. Lett.* **100**, 053107 (2012).
- [17] F. Lange, O. Ernst, T. Teubner, C. Richter, M. Schmidbauer, O. Skibitzki, T. Schroeder, P. Schmidt, and T. Boeck, In-plane growth of germanium nanowires on nanostructured Si(001)/SiO₂ substrates, *Nano Futures* **4**, 035006 (2020).
- [18] D. Zubia, S. H. Zaidi, S. D. Hersee, and S. R. J. Brueck, Nanoheteroepitaxy: Nanofabrication route to improved epitaxial growth, *J. Vac. Sci. Technol. B: Microelectron. Nanometer Struct.* **18**, 3514 (2000).
- [19] D. Zubia and S. D. Hersee, Nanoheteroepitaxy: The application of nanostructuring and substrate compliance to the heteroepitaxy of mismatched semiconductor materials, *J. Appl. Phys.* **85**, 6492 (1999).
- [20] G. Niu, G. Capellini, M. A. Schubert, T. Niermann, P. Zaumseil, J. Katzer, H. M. Krause, O. Skibitzki, M. Lehmann, Y. H. Xie *et al.*, Dislocation-free Ge nano-crystals via pattern independent selective Ge heteroepitaxy on Si nano-tip wafers, *Sci. Rep.* **6**, 22709 (2016).
- [21] G. Niu, G. Capellini, F. Hatami, A. Di Bartolomeo, T. Niermann, E. H. Hussein, M. A. Schubert, H. M. Krause, P. Zaumseil, O. Skibitzki *et al.*, Selective epitaxy of InP on Si and rectification in graphene/InP/Si hybrid structure, *ACS Appl. Mater. Interfaces* **8**, 26948 (2016).
- [22] G. Niu, S. J. Leake, O. Skibitzki, T. Niermann, J. Carnis, F. Kiessling, F. Hatami, E. H. Hussein, M. A. Schubert, P. Zaumseil *et al.*, Advanced coherent x-ray diffraction and electron microscopy of individual InP nanocrystals on Si nanotips for III-V-on-Si electronics and optoelectronics, *Phys. Rev. Appl.* **11**, 064046 (2019).
- [23] L. Lemmo, A. di Bartolomeo, F. Giubileo, G. Luongo, M. Passacantando, G. Niu, F. Hatami, O. Skibitzki, and T. Schroeder, Graphene enhanced field emission from InP nanocrystals, *Nanotechnology* **28**, 495705 (2017).
- [24] O. Skibitzki, I. Prieto, R. Kozak, G. Capellini, P. Zaumseil, Y. Arroyo Rojas Dasilva, M. D. Rossell, R. Erni, H. von Kanel, and T. Schroeder, Structural and optical characterization of GaAs nano-crystals selectively grown on Si nano-tips by MOVPE, *Nanotechnology* **28**, 135301 (2017).
- [25] R. A. B. Devine, D. Mathiot, W. L. Warren, D. M. Fleetwood, and B. Aspar, Point defect generation during high temperature annealing of the Si-SiO₂ interface, *Appl. Phys. Lett.* **63**, 2926 (1993).
- [26] R. A. B. Devine, D. Mathiot, W. L. Warren, and B. Aspar, O interstitial generation and diffusion in high temperature annealed Si/SiO₂/Si structures, *J. Appl. Phys.* **79**, 2302 (1996).
- [27] D. Spirkoska, J. Arbiol, A. Gustafsson, S. Conesa-Boj, F. Glas, I. Zardo, M. Heigoldt, M. H. Gass, A. L. Bleloch, S. Estrade *et al.*, Structural and optical properties of high quality zinc-blende/wurtzite GaAs nanowire heterostructures, *Phys. Rev. B: Condens. Matter Mater. Phys.* **80**, 245325 (2009).
- [28] K. Ikejiri, Y. Kitauchi, K. Tomioka, J. Motohisa, and T. Fukui, Zinc blende and wurtzite crystal phase mixing and transition in indium phosphide nanowires, *Nano Lett.* **11**, 4314 (2011).
- [29] J. Vukajlovic-Plestina, W. Kim, L. Ghisalbetti, G. Varnavides, G. Tütüncüoglu, H. Potts, M. Friedl, L. Güniat, W. C. Carter, V. G. Dubrovskii *et al.*, Fundamental aspects to localize self-catalyzed III-V nanowires on silicon, *Nat. Commun.* **10**, 869 (2019).
- [30] H. Zeng, X. Yu, H. A. Fonseka, G. Boras, P. Jurczak, T. Wang, A. M. Sanchez, and H. Liu, Preferred growth direction of III-V nanowires on differently oriented Si substrates, *Nanotechnology* **31**, 475708 (2020).
- [31] M. D. Abràmoff, P. J. Magalhães, and S. J. Ram, Image processing with ImageJ, *Biophotonics Int.* **11**, 36 (2004).
- [32] P. Zaumseil, High-resolution characterization of the forbidden Si 200 and Si 222 reflections, *J. Appl. Crystallogr.* **48**, 528 (2015).
- [33] *Semiconductors: Group IV Elements and III-V Compounds*, edited by O. Madelung (Springer, Berlin, Heidelberg, 1991).
- [34] M. W. Larsson, J. B. Wagner, M. Wallin, P. Håkansson, L. E. Fröberg, L. Samuelson, and L. R. Wallenberg, Strain mapping in free-standing heterostructured wurtzite InAs/InP nanowires, *Nanotechnology* **18**, 015504 (2007).
- [35] M. Neubert, A. Kwasniewski, and R. Fornari, Analysis of twin formation in sphalerite-type compound semiconductors: A model study on bulk InP using statistical methods, *J. Cryst. Growth* **310**, 5270 (2008).
- [36] B. Jiming, D. C. Bell, F. Capasso, J. B. Wagner, T. Mårtensson, J. Trägårdh, and L. Samuelson, Optical properties of rotationally twinned InP nanowire heterostructures, *Nano Lett.* **8**, 836 (2008).
- [37] A. J. Lohn, T. Onishi, and N. P. Kobayashi, Optical properties of indium phosphide nanowire ensembles at various temperatures, *Nanotechnology* **21**, 355702 (2010).
- [38] E. G. Gadret, M. M. De Lima, J. R. Madureira, T. Chiamonte, M. A. Cotta, F. Iikawa, and A. Cantarero, Optical phonon modes of wurtzite InP, *Appl. Phys. Lett.* **102**, 122101 (2013).
- [39] A. Mooradian and G. B. Wright, First order Raman effect in III-V compounds, *Solid State Commun.* **4**, 431 (1966).
- [40] M. Chashnikova, A. Mogilatenko, O. Fedosenko, V. Bryksa, A. Petrov, S. MacHulik, M. P. Semtsiv, W. Neumann, and W. T. Masselink, Growth and properties of self-assembled InP-nanoneedles on (0 0 1) InP by gas source MBE, *J. Cryst. Growth* **323**, 319 (2011).
- [41] I. Vurgaftman, J. R. Meyer, and L. R. Ram-Mohan, Band parameters for III-V compound semiconductors and their alloys, *J. Appl. Phys.* **89**, 5815 (2001).
- [42] A. De and C. E. Pryor, Predicted band structures of III-V semiconductors in the wurtzite phase, *Phys. Rev. B: Condens. Matter Mater. Phys.* **81**, 155210 (2010).
- [43] A. Zilli, M. De Luca, D. Tedeschi, H. A. Fonseka, A. Miriametro, H. H. Tan, C. Jagadish, M. Capizzi, and A. Polimeni, Temperature dependence of interband transitions in wurtzite InP nanowires, *ACS Nano* **9**, 4277 (2015).
- [44] T. Akiyama, K. Sano, K. Nakamura, and T. Ito, An empirical potential approach to wurtzite-zinc-blende polytypism in group III-V semiconductor nanowires, *Jpn. J. Appl. Phys. Part 2* **45**, L275 (2006).
- [45] H. J. Chu, T. W. Yeh, L. Stewart, and P. D. Dapkus, Wurtzite InP nanowire arrays grown by selective area MOCVD, *Phys. Status Solidi C* **7**, 2494 (2010).
- [46] P. Caroff, K. A. Dick, J. Johansson, M. E. Messing, K. Deppert, and L. Samuelson, Controlled polytypic and twin-

- plane superlattices in III-V nanowires, *Nat. Nanotechnol.* **4**, 50 (2009).
- [47] S. Paiman, Q. Gao, H. H. Tan, C. Jagadish, K. Pemasiri, M. Montazeri, H. E. Jackson, L. M. Smith, J. M. Yarrison-Rice, X. Zhang *et al.*, The effect of V/III ratio and catalyst particle size on the crystal structure and optical properties of InP nanowires, *Nanotechnology* **20**, 225606 (2009).
- [48] K. P. O'Donnell and X. Chen, Temperature dependence of semiconductor band gaps, *Appl. Phys. Lett.* **58**, 2924 (1991).
- [49] Z. Su, N. Wang, H. H. Tan, and C. Jagadish, 2D carrier localization at the wurtzite-zincblende interface in novel layered InP nanomembranes, *ACS Photonics* **8**, 1735 (2021).
- [50] Q. Gao, D. Saxena, F. Wang, L. Fu, S. Mokkaapati, Y. Guo, L. Li, J. Wong-Leung, P. Caroff, H. H. Tan *et al.*, Selective-area epitaxy of pure wurtzite InP nanowires: High quantum efficiency and room-temperature lasing, *Nano Lett.* **14**, 5206 (2014).
- [51] M. De Luca and A. Polimeni, Electronic properties of wurtzite-phase InP nanowires determined by optical and magneto-optical spectroscopy, *Appl. Phys. Rev.* **4**, 041102 (2017).
- [52] I. Geijselaers, S. Lehmann, K. A. Dick, and M.-E. Pistol, Two-dimensional electron gas at wurtzite-zinc-blende InP interfaces induced by modulation doping, *Appl. Phys. Lett.* **116**, 232103 (2020).
- [53] F. Hatami, N. N. Ledentsov, M. Grundmann, J. Böhrer, F. Heinrichsdorff, M. Beer, D. Bimberg, S. S. Ruvimov, P. Werner, U. Gösele *et al.*, Radiative recombination in type-II GaSb/GaAs quantum dots, *Appl. Phys. Lett.* **67**, 656 (1995).
- [54] P. E. Faria Junior and G. M. Sipahi, Band structure calculations of InP wurtzite/zinc-blende quantum wells, *J. Appl. Phys.* **112**, 103716 (2012).
- [55] G. L. Tuin, M. T. Borgström, J. Trägårdh, M. Ek, R. R. Wallenberg, L. Samuelson, and M. E. Pistol, Valence band splitting in wurtzite InP nanowires observed by photoluminescence and photoluminescence excitation spectroscopy, *Nano Res.* **4**, 159 (2011).
- [56] K. Li, H. Sun, F. Ren, K. W. Ng, T. T. D. Tran, R. Chen, and C. J. Chang-Hasnain, Tailoring the optical characteristics of microsized InP nanoneedles directly grown on silicon, *Nano Lett.* **14**, 183 (2014).
- [57] A. Mishra, L. V. Titova, T. B. Hoang, H. E. Jackson, L. M. Smith, J. M. Yarrison-Rice, Y. Kim, H. J. Joyce, Q. Gao, H. H. Tan *et al.*, Polarization and temperature dependence of photoluminescence from zincblende and wurtzite InP nanowires, *Appl. Phys. Lett.* **91**, 263104 (2007).